frontiers | Frontiers in Physics

TYPE Original Research
PUBLISHED 22 June 2023
DOI 10.3389/fphy.2023.1167927

OPEN ACCESS

EDITED BY
Marco La Cognata,
Laboratori Nazionali del Sud (INFN), Italy

REVIEWED BY
Giovanni Luca Guardo,
Laboratori Nazionali del Sud (INFN), Italy
Zhao Yongtao,
Xi'an Jiaotong University, China

*CORRESPONDENCE
Tongjun Xu,
tjxu@siom.ac.cn
Guoqiang Zhang,
zhangguoqiang@sari.ac.cn
Liangliang Ji,
jill@siom.ac.cn

RECEIVED 17 February 2023
ACCEPTED 12 June 2023
PUBLISHED 22 June 2023

CITATION
Fan L, Xu T, Wang Q, Xu J, Zhang G, Wang P, Fu C, Ma Z, Deng X, Ma Y, Li S, Lu X, Li J, Xu R, Wang C, Liang X, Leng Y, Shen B, Ji L and Li R (2023), Enhanced laser-driven backward proton acceleration using micro-wire array targets.
Front. Phys. 11:1167927.
doi: 10.3389/fphy.2023.1167927

Enhanced laser-driven backward proton acceleration using micro-wire array targets

Lulin Fan[1,2], Tongjun Xu[1]*, Qingsong Wang[1], Jiancai Xu[1], Guoqiang Zhang[3,4]*, Putong Wang[2,3], Changbo Fu[5], Zhiguo Ma[5], Xiangai Deng[5], Yugang Ma[5], Shun Li[1], Xiaoming Lu[1], Jinfeng Li[1], Rongjie Xu[1], Cheng Wang[1], Xiaoyan Liang[1], Yuxin Leng[1], Baifei Shen[1,6], Liangliang Ji[1]* and Ruxin Li[1,7]

[1]State Key Laboratory of High Field Laser Physics and CAS Center for Excellence in Ultra-intense Laser Science, Shanghai Institute of Optics and Fine Mechanics, Chinese Academy of Sciences, Shanghai, China, [2]Center of Materials Science and Optoelectronics Engineering, University of Chinese Academy of Sciences, Beijing, China, [3]Shanghai Institute of Applied Physics, Chinses Academy of Sciences, Shanghai, China, [4]Shanghai Advanced Research Institute, Chinese Academy of Sciences, Shanghai, China, [5]Key Laboratory of Nuclear Physics and Ion-Beam Application (MOE), Institute of Modern Physics, Fudan University, Shanghai, China, [6]Department of Physics, Shanghai Normal University, Shanghai, China, [7]School of Physical Science and Technology, ShanghaiTech University, Shanghai, China

Micro-structured targets can be employed to enhance the coupling of laser energy to the high energy density plasma. Here we report on experimental measurement of enhanced proton beam energy from laser-driven micro-wire array (MWA) targets along the backward direction. An ultra-intense (~ 2×10^{20}W/cm^2) laser pulse of ~ 40 fs pulse duration interacts with the MWA structure and induces large population of energetic electrons. The enhanced sheath field efficiently accelerates protons both transversely and longitudinally. The spectrometers record proton cut-off energy of around 16 MeV and temperature 813keV along the backward direction, which is 20% – 60% higher than that of a flat target under commensurate laser conditions. Comparison with particle-in-cell simulations suggests that the enhancement originates from the increased temperature and population of the hot electrons within the micro-wires. These measurements provide a direct probe of the high energy density plasma condition in laser-driven solid targets and a useful benchmark for further studies on laser-driven micro-structured targets.

KEYWORDS

laser-proton acceleration, micro-wire structure, high laser-proton energy coupling efficiency, high energy density plasma, laser-induced nuclear fusion

Introduction

In the past 2 decades, laser-driven proton acceleration has been developed as a new acceleration method. Due to the high peak flux, short pulse duration and small beam size, laser-driven proton sources are promising in various key applications, such as proton therapy [1], high energy density physics, fast ignition [2] and laboratory astrophysics [3]. Several acceleration mechanisms have been studied to produce high energy protons, including the target normal sheath acceleration [4, 5] (TNSA), shock wave acceleration [6], the radiation pressure acceleration [7] (RPA) *etc.* While many proposals suggested proton energies could reach up to GeV level, the state-of-art experimental value is around

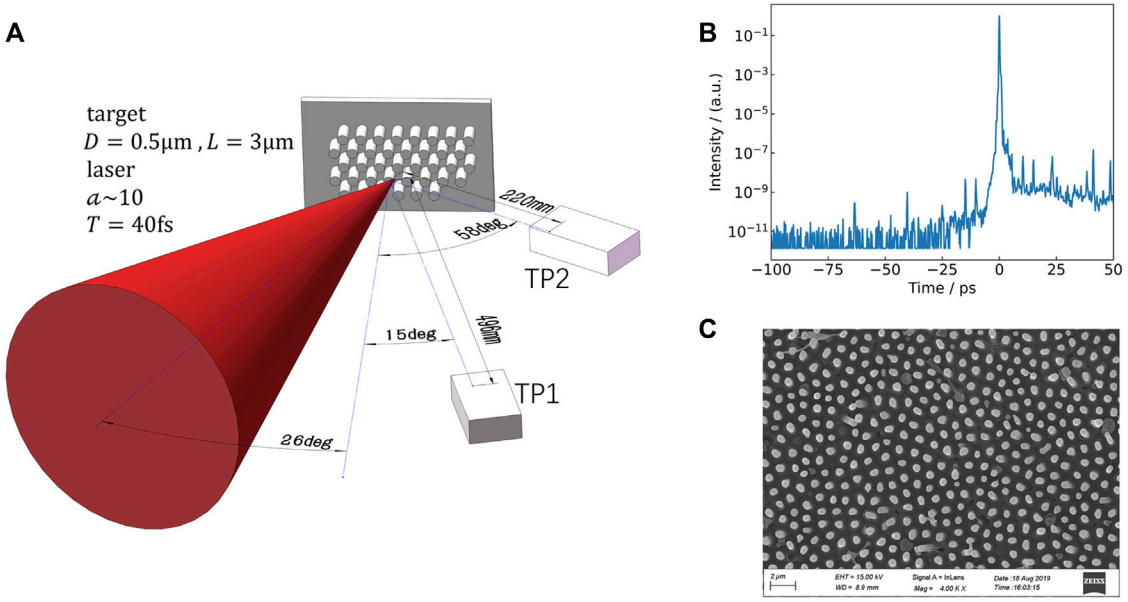

FIGURE 1
(A) Schematic of experimental setup. The laser pulse with a = 10 is incident on the micro-wire target. **(B)** Contrast measurements with a third-order scanning cross-correlator [34]. **(C)** SEM image of the micro-wire target with the wire diameters(D) of 0.5μm, the lengths(L) of 3μm.

100 MeV based on TNSA [8] or hybrid scheme of radiation pressure-sheath acceleration [9]. The gap between them has led to continuous efforts in raising the proton energies based on realistic laser conditions, including improved target designs such as 'snow flake' [10], grating [11], nanotube foam [12], nanospheres [13], micro-wire arrays [14], nanochannels [15] and even bacteria [16], among which an important direction is using micro-structured targets. For example, micro-wire array (MWA) targets have been proposed to enhance laser energy conversion efficiency into not only energetic ions [17–21], but also electrons [22–24], x-ray emission [25, 26], and positrons [27].

When an ultrahigh contrast femtosecond laser penetrates deep into the MWA, it creates a large volumetrically heated plasma [24–26], which is the major reason for the high-efficiency generation of x-rays and relativistic electrons. Further, the electrons within the wires are pulled out by the laser field and accelerated via direct laser acceleration (DLA) [28], leading to substantial enhancement in both the population and energies of the produced electron beam [23]. These together benefit acceleration of high energy protons via enhanced sheath field [20]. The laser energy is thus efficiently coupled into energetic protons and therefore can be employed to boost the fusion reaction in the vicinity of high energy density plasma [21, 29]. In this case, the substrates of some MWA targets are usually quite thick to maximize the fusion reaction events [21, 22]. Sheath field at the target rear surface cannot be formed efficiently, thus measuring protons or energetic ions accelerated at the target rear becomes challenging. For this reason, detection of the protons emitted from the front surface turns to be a direct approach to obtain information of interaction regions in micro-structured targets. It has been reported that 13 MeV deuterium ions were measured in the laser beam backward direction by irradiating a deuterated nanowire target with a high contrast strong laser, and the highest proton energy was 7.25 MeV [21].

Some experiments [30, 31] find an almost symmetric behavior for protons accelerated from rear and front sides with the laser intensity range 10^{18}W/cm^2 – 10^{20}W/cm^2 and the contrast ratio close to 10^{10}, which is interpreted on the basis that similar sheath fields are built on both target surfaces. However, in the case of laser intensity 2×10^{20}W/cm^2 – 10^{21}W/cm^2 and pulse temporal contrast ~ 10^{10} (a few ps prior to the main pulse), an imbalance between forward and backward proton acceleration was observed [32, 33]. The maximum energy of the forward accelerated protons is about 10 MeV higher than that of the backward accelerated protons. Such a strong asymmetry in proton energies may be induced by the constrained electron expansion and electrostatic field generation at the target front. Using a laser of 8×10^{20}W/cm^2 to irradiate 6 μm thick Al foil targets at an angle of incidence 30°, the cut-off energy of protons observed in front of the target is 18MeV [33]. Compared with the forward accelerated protons, the backward accelerated protons are not affected by the interaction with the bulk target substrate, so their properties can be easily referred to the interaction region.

In this paper, using a laser with a peak intensity of 2×10^{20}W/cm^2 to interact with MWA targets, a proton beam with cut-off energy of 16 MeV was measured at the target front, which is 20% – 60% higher than that of a flat target under commensurate laser conditions. The results are well interpreted by particle-in-cell (PIC) simulations, showing that laser-proton energy coupling efficiency is enhanced due to the volumetric heating of the micro-wire. Such interaction will significantly benefit laser-induced nuclear fusion with micro-structures.

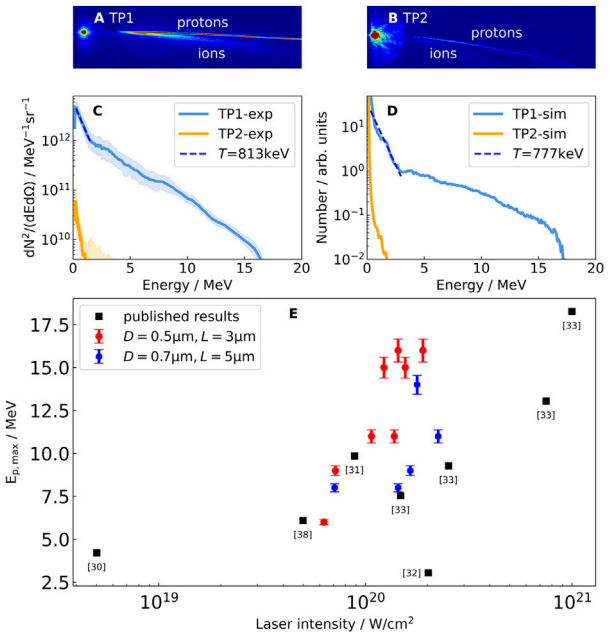

FIGURE 2
(A), **(B)** The raw IP data of TP1 and TP2 respectively. **(C)** Experiment energy spectrum of the proton in front of the target with a wire diameter of 0.5μm and a wire length of 3μm at an angle of 15° 58° to the target normal direction **(D)** Simulation energy spectrum of the proton in front of the target at an angle of $\cos 15° \pm 0.033 \cos 58° \pm 0.033$ to the target normal direction while maintaining the same average density with **(C)**. The shaded regions represent uncertainty. **(E)** Cut-off energies of backward TNSA-accelerated protons with short pulses ($\tau < 60$fs) and target thicknesses greater than 0.1μm. The published results are taken from the reference shown in square brackets. The error bars are defined by the uncertainty in maximum proton energy arising from the energy resolution of the Thompson spectrometer.

Experimental results

The experiment was carried out on a femtosecond petawatt laser system at Shanghai Institute of Optics and Fine Mechanics (SIOM), which delivered laser beams with a central wavelength of $\lambda = 800$nm and a duration of 40 fs. This Ti-Sapphire laser is based on the standard chirped-pulse-amplification (CPA) technique. The 10 – 20j laser energy was focused to a 10 μm full width at half maximum (FWHM) focal spot with an F/4 off-axis parabola, reaching a peak intensity $\sim 2 \times 10^{20}$W/cm^2. The corresponding normalized laser amplitude is $a = 10$ ($a = eE/m_e c\omega$), where e and m_e are the electron charge and mass, E is the laser electric field, ω is the laser frequency, and c is the speed of light in vacuum, respectively. The contrast of amplified spontaneous emission (ASE) pedestal is 10^{11} (10^{10}) at 30(6)ps prior to the main pulse [34] shown in Figure 1B, which could induce pre-plasmas with typical scale length of several tens of nanometers.

The schematic diagram of the experiment is shown in Figure 1A. The p-polarized laser pulse is incident on the target surface at an angle of −26°. Two Thompson spectrometers (shown as TP1 and TP2) are placed at distances of 49.6 cm and 22 cm from the target point at angles of 15° and 58° incident angles to the target normal, respectively. There is a aperture with a diameter of 100 μm in front of the two spectrometers to avoid signal saturation, and the corresponding solid angles for ion collection was 3.2×10^{-8}Sr and 1.6×10^{-7}Sr. Ion information is recorded by image plates (IPs). Here the normal direction at the target front is occupied to detect fusion signals, which will be described in the future work.

The target is made of a mixture material of polyethylene and boroncarbide powder, with the mass ratio of 1.86: 1. Micro-wires are fabricated by the Anodized Aluminum Oxide (AAO) template [35]. After fully mixing polyethylene and boron powder, the target material enters the AAO template by heating and extrusion, and decomposes with NaOH solution for 30 min. The micro-wires are supported by 100 – 300 μm thick mixture substrate, while the wire diameter, length and spacing are determined by the AAO template. The distance between the wires is 0.8 μm for both types of targets used in the experiment, with the wire diameters(D) of 0.5 um as seen in the scanning electron microscope (SEM) image in Figure 1C and 0.7 um, the lengths(L) of 3 μm and 5 μm, corresponding to average densities of 35.4% and 69.4% of the intrinsic material density, respectively. In the experiment, the MWA targets were fixed on a glass substrate with a thickness of 3.5 mm. In addition, the proton-boron fusion is also measured, which will be discussed in the future work.

The recorded parabolic ion traces on IPs shown in Figure 2A and Figure 2B were analyzed using a MATLAB code applying an existing scaling relationship [36]. Figure 2C shows the proton energy spectra with a wire diameter of 0.5 μm and length of 3μm. Maximum proton energy of 16 MeV was measured at an angle of 15° to the target normal direction (TP1). The spectra show an approximately exponential decay in the low-energy region, $n(E) \sim n_0 \exp(-E/T_{\text{eff}})$, with an effective temperature $T_{\text{eff}} \approx 813$keV. This is beneficial to increase the nuclear reaction rate of hydrogen and boron, which is related to the densities n and

TABLE 1 Laser-driven backward proton acceleration results are shown in comparison with previous experiments.

	Laser FWHM (fs)	Laser intensity (W/cm^2)	Target thickness (μm)	Proton energy (MeV)
Bychenkov et al [33]	30	8×10^{20}	6	18
Ceccotti et al [30]	65	5×10^{18}	0.08–105	4.2
Fourmaux et al [31]	30	8.9×10^{19}	0.015–50	9.6
Prasad et al [32]	50	2×10^{20}	0.05–10	3
Schnurer et al [38]	45	5×10^{19}	0.029–0.05	6.1
This work	40	$\sim 2 \times 10^{20}$	—	16

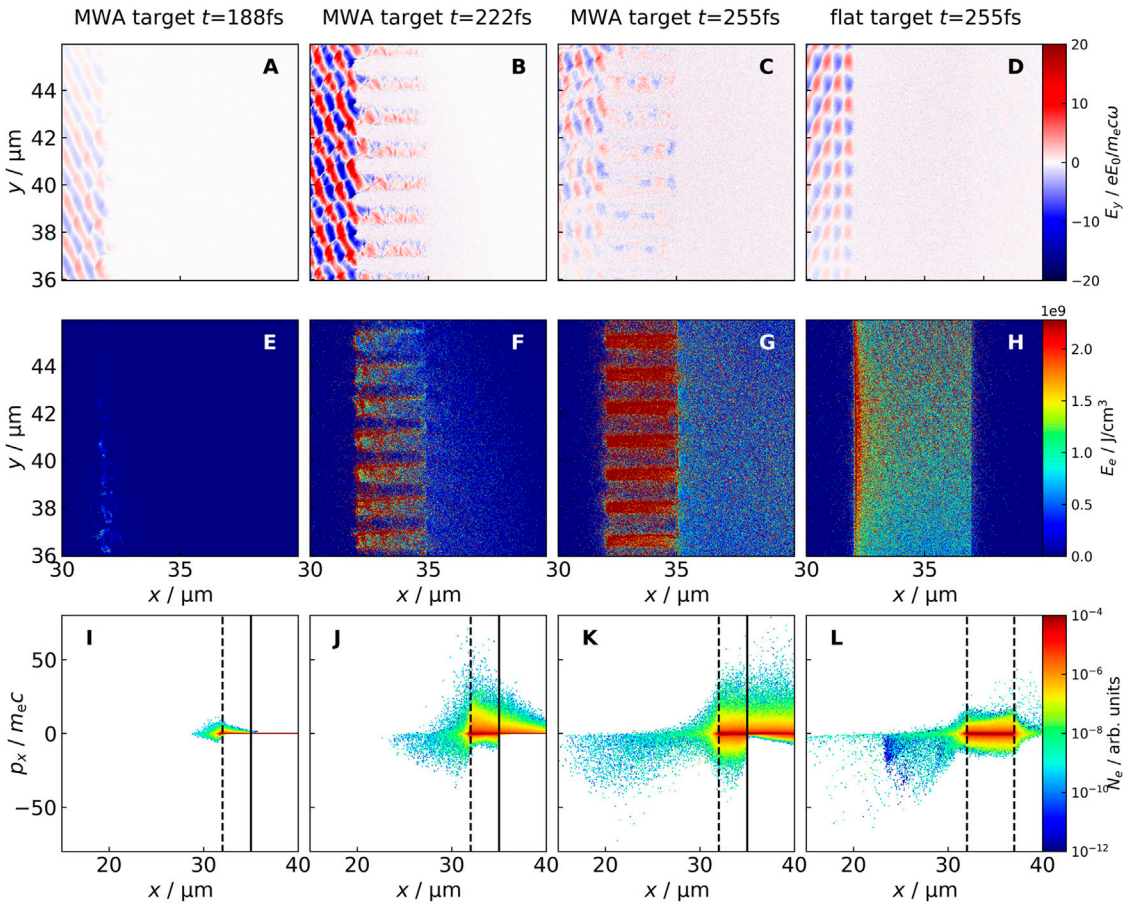

FIGURE 3
2D PIC simulations results. **(A–C)** Spatial distribution of the electric field E_y and the electron energy density **(E–G)** and the $x - p_x$ phase of electrons **(I–K)** at the simulation time t = 188fs, 222fs, 255fs for the micro-wire target. The MWA is between the dotted line and the solid line in **(I–K)**. (d)Spatial distribution of the electric field E_y and the electron energy density(h) and the $x - p_x$ phase of electrons **(L)** at the simulation time t = 255fs for flat target. The flat target is between the dotted line and the dotted line. **(A–H)** have same scale and label.

relative velocity v of two reacting species, $R \sim n_1 n_2 < \sigma v > \sim n_1 n_2 T^{\alpha}$. Here σ is cross section, T is temperature and $\alpha \sim 3 - 4$ for light ion reactions in the temperature range of 10 – 30keV [37]. As the reflection angle increases (TP2), both the proton cut-off energy and population decrease significantly, indicating the dominance of TNSA mechanism.

The current experiment did not consider the case for flat foils. However, one could refer to previous results with similar laser conditions. In Ref. [30–33, 38], flat foils of thickness >0.1 μm were irradiated by laser pulse shorter than 60 fs at various laser intensities. The cut-off energies of backward TNSA-accelerated protons are listed in Figure 2E. In the range of $0.5 - 2 \times 10^{20}$W/cm^2, one finds that the MWA targets employed here produce maximum energies 20% – 60% higher than that of flat targets shown in Table1. We also include the results with a wire diameter of 0.7 μm and a length of 5 μm in Figure 2E, which show consistent enhancement as compared to the flat targets. The maximum proton energy is slightly lower than that for D = 0.5μm and L = 3μm owing to its higher average density when laser impinges onto the structure.

Simulation results

We use the particle-in-cell (PIC) program SMILEI [39] to interpret the experimental observation. Due to the demanding computation requirement for simulating dense micro-structures, we restrict our simulations to two-dimensional (2D) geometry. Based on the test simulations, we found that the proton acceleration saturates at about 500 fs, corresponding to roughly 40 μm. Thus, the longitudinal length of the simulation box is 40 μm. The y dimension of the simulation box is set to 81.92 μm, following the rule in SMILEI simulation (λ = 0.8 μm is the laser wavelength). The cell size of 10nm × 10nm and the time-step of 0.022fs is set to fulfill the resolution requirement of convergent simulation results and balance the computational cost. The number of macro-particles per cell to 16 for all simulations. A linearly polarized laser with a peak intensity of a = 10 and a focal spot of 10μm (FWHM) is incident on the target surface at an angle of −26°, consistent with the experimental conditions. The number ratio of C^{6+} and H^+ in simulated target is 1: 2, and the total electron density is $80n_c$. Here $n_c = (\varepsilon_0 m_e \omega^2)/e^2 = 1.7 \times 10^{21}$cm^{-3} is the critical

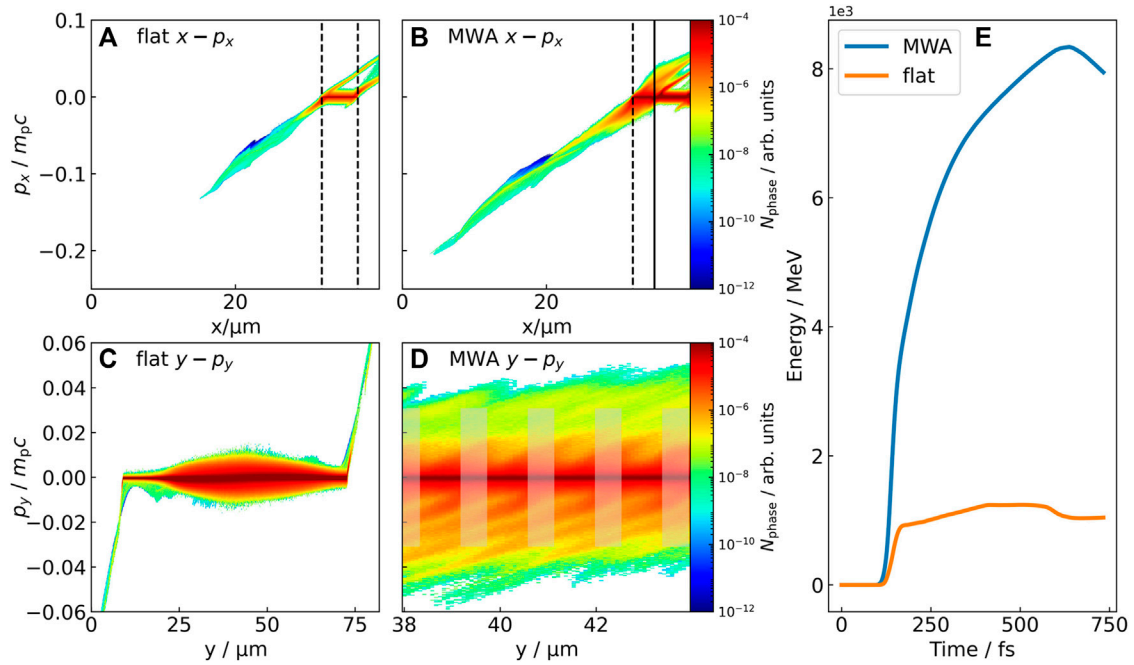

FIGURE 4
The $x-p_x$ and $y-py$ phase spaces of the protons for the flat target **(A) (C)** and the MWA target **(B) (D)** at t = 777fs. The flat target is between the dotted line and the dotted line in **(A)**, the MWA is between the dotted line and the solid line in **(B)**, MWA are represented by gray transparent stripes in **(D)**. **(E)** Proton total energy over the simulation time for the flat target and MWA target.

electron number density, where ε_0 is the vacuum permittivity. The initial temperature of each species is 1eV. The substrate is located at 35μm < x < 40μm, where x = 40μm is the right boundary of the simulation window. We employ absorbing boundary conditions for particles. Considering the influence of the pre-pulse of the laser, we set a neutral pre-plasma with an electron density of $80n_c \exp(-d/L_0)$ on the front surface of the wire target, which extends to 3μm at the target front, where L_0 is the density scale length and d is the distance to the target surface. Considering the initial temperature of the target in our simulation and the laser conditions in our experiment, we estimate $L_0 = c_s t_p$ = 60nm, where c_s and t_p are ion sound velocity and pre-pulse duration [40]. To maintain the same average density as in the experiment, wire period (P) of the MWA in the 2D simulation is set to 1.4 μm, while diameter of 0.5 μm, length of 3 μm remain the same, and the base thickness is set as 5 μm. The thickness of the flat target is 5 μm, and the front surface is located at x = 32μm.

The electric field E_y distributions in Figures 3A–C show that a femtosecond laser pulse can penetrate deeply into the wire array. Compared with the flat target shown in Figure 3D, the MWA target has a larger contact area with the laser. The transverse E_y field extracts the electrons from the wire, which either quiver across the density gradient region or move longitudinally under the effect of relativistic $J \times B$ force. The ultrashort duration of the laser pulse allows for the majority of the energy to be efficiently deposited before gap closure such that the thermal energy density of the plasma is significantly enhanced via volumetric heating [26], as shown in Figures 3E–G. The maximum energy density of electrons in micro-wires is 6.4×10^{10}J/cm^3, which is twice that of flat target at t = 255fs shown in Figure 3H under same laser conditions. The energetic electrons escape from the target front surface and establish space-charge sheath [22]. Compared with the flat target (Figure 3L), the population of hot electrons (Figures 3I–K) for the MWA target is significantly increased. These all together lead to efficient proton acceleration. The proton energy spectra and the cut-off energies from PIC simulations agree well with the experimental results, as already illustrated in Figures 2C, D.

Figures 4A–D describes the $x-p_x$ and $y-p_y$ phase distribution of protons for the flat target and MWA target. The longitudinal momenta of protons in MWA are notably higher than that of the flat target as seen in Figures 4A, B, a natural result from the enhanced sheath field driven by large population of high energy electrons from the surface. An interesting phenomenon revealed in Figure 4D is that the protons also gain significant transverse momenta, reaching 25% of the longitudinal one. Apparently, the expanding electrons also build up huge sheath field perpendicular to target normal direction. These protons are confined between MWA units shown in Figure 2D, corresponding to an effective temperature at 777keV. This is beneficial to increase the nuclear reaction rate R of hydrogen and boron. The boosted nuclear reaction with MWA structures has also been verified in experiment and will be discussed in an independent work.

In Figure 4E we compare the total proton energy obtained from the laser. The energy conversion tends to saturated after 500 fs away from the beginning of the interaction for the MWA targets, while it only take 50 fs for the flat targets. The total energy obtained from the laser by protons (>1 MeV) at the target front is 6 times higher than the flat target for the MWA target.

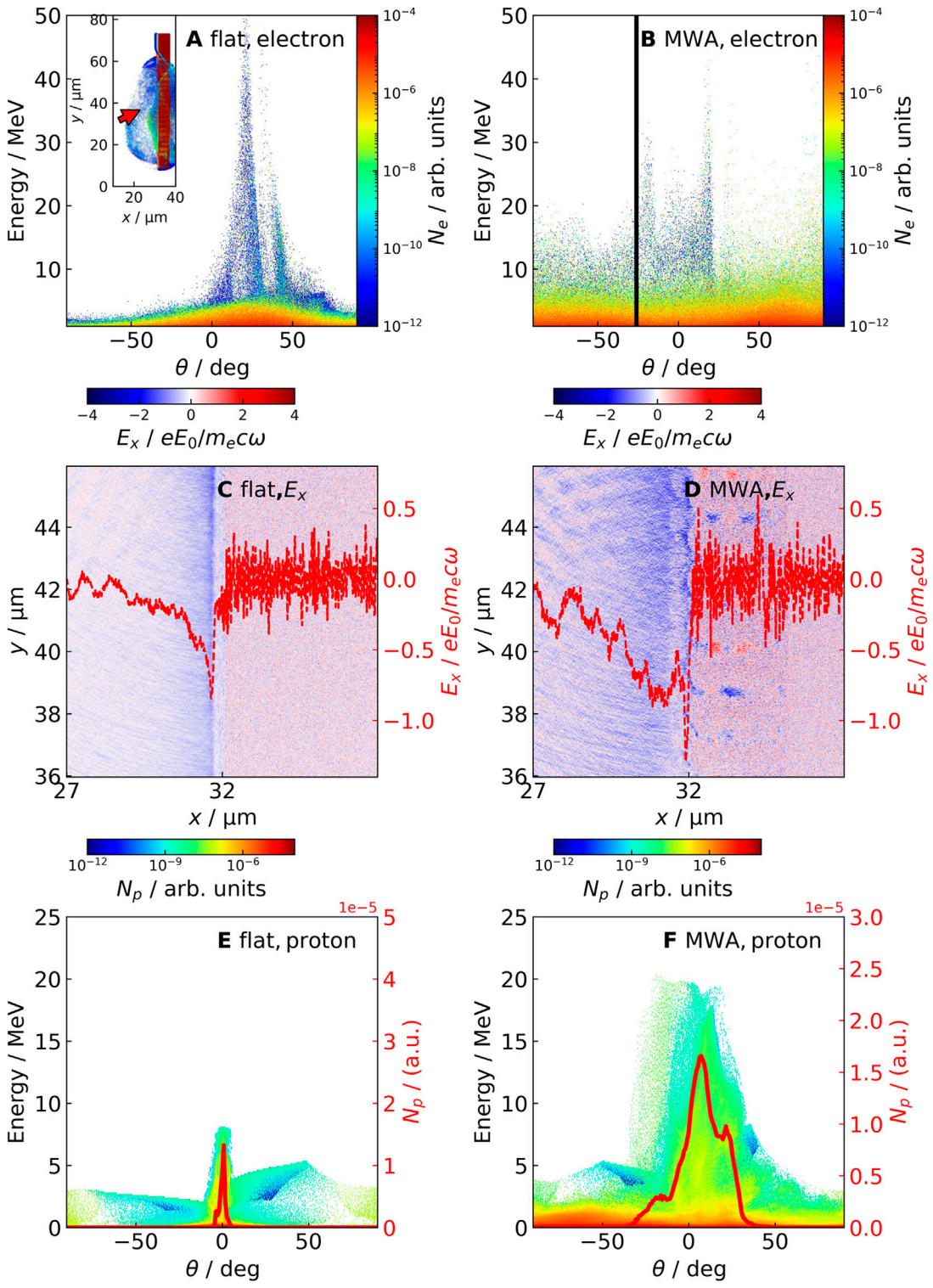

FIGURE 5
The angular-energy distribution of electrons in **(A)** flat target, **(B)** micro-wire target at t = 255 fs. Spatial distribution of the electric field E_x at the simulation time t = 288 fs for the flat target **(C)** and the micro-wire target **(D)**. The red line shows the sheath field along the x-axis at y = 43 µm. The angular-energy distribution of protons in **(E)** flat target, **(F)** micro-wire target at t = 777 fs. The electrons density distribution for the flat target is shown in the inset of **(A)**. The red arrow in the inset of **(A)** and the solid line in **(B)** is the direction of the incident laser. The red line in **(E)** and **(F)** represent the angular distribution of the protons above 5 MeV.

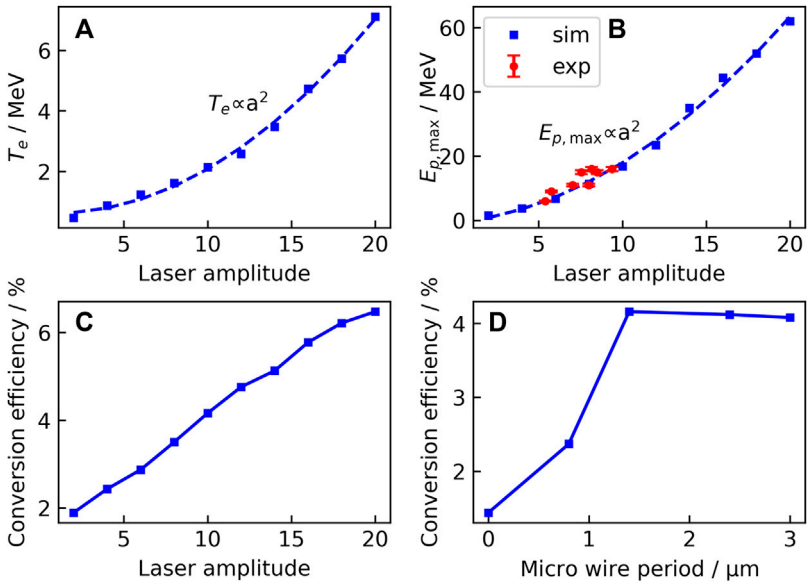

FIGURE 6
(A) The scaling law of laser amplitude and electron temperature. **(B)** The experiment (red) and simulation (blue) scaling law of laser intensity versus proton maximum energy. The error bars are defined by the uncertainty in maximum proton energy arising from the energy resolution of the Thompson spectrometer. The distance between the wires is 0.8 μm for the target used in the experiment, with the wire diameters(D) of 0.5 um and length(L) of 3 μm. Energy conversion efficiency as a function of laser amplitude **(C)** and micro wire period **(D)**. The micro wire period of 0 means a flat target.

The relative number density distributions of electrons and protons in the energy-angle domain are presented in Figure 5. One can see that there is a gap at 26° for both the flat and micro-wire targets in Figures 5A, B. It is related to the fact that the electrons are expelled by the ponderomotive force of the reflected laser shown as the inset of Figure 5A. The total number of electrons with energy above 1MeV for the MWA target shown in Figure 5B is 8 times that of the flat target shown in Figure 5A. The TNSA field is enhanced approximately twice by these electrons shown in Figures 5C, D. The total number and maximum energy of the proton beam are also increased for the MWA target through the enhanced TNSA field (Figures 5E, F), which is consistent with Figures 4A, B. Applying the scaling law of ion cut-off energy versus hot electron temperature $E_{ion} = \alpha T_{hot}$ [5, 41], we find a value of $\alpha \sim 6.6$, which is consistent with previous report [21]. The angular distribution of the protons above 5 MeV is denoted by the red line in Figures 5E, F. For the MWA target, the proton divergence angle (FWHM) is 25° but only 1.8° for the flat target. This is because the transverse momentum of most protons is relatively large for MWA target shown in Figure 4F. It is interesting to notice that the proton energy spectrum exhibits asymmetry profiles, where protons are deflected along the direction of the reflected laser. This is because the oblique incidence of the laser pulse induces a large number of electrons deviate from the normal direction of the target.

Discussion

An important feature of the MWA structure is the promising scaling law $E_{ion\_max} \propto a^2$ between the laser intensity and proton cut-off energy, which is different for standard TNSA mechanism $E_{ion\_max} \propto a$, as shown in Figure 6B. This is possibly because the high energy electrons are generated via direct laser acceleration rather than ponderomotive acceleration for flat surfaces, which generate higher temperature shown in Figure 6A. The former provides a more efficient scaling with respect to the laser field [23] than the latter. This trend is observed in experiment from $a = 5 \sim 10$ due to the limitation of the laser system. PIC simulations reproduce the results in this range and indicate that it can be extended to laser intensities approaching $a = 20$. For even higher intensities, the scaling law may come to saturation, as pointed out by previous simulations using micro-channel structures [42]. Such behavior is yet to be confirmed in experiment. Energy conversion efficiency increases with the increase of laser amplitude as shown in Figure 6C. The energy conversion efficiency increases first and then decrease when the micro wire period is increased as shown in Figure 6D. The MWA target is close to the flat target when the period is large, and the laser cannot enter between the wires when the period is small, so the energy coupling efficiency decreases.

Conclusion

We report on experimental measurement of proton beams with maximum energy of 16 MeV accelerated by a target normal sheath acceleration (TNSA) field at the target front, and confirm the enhanced effect of MWA on the acceleration of protons in front side of the target in the experiment. It can be found by simulation that the enhancement originates from the increased temperature and population of the hot electrons within the micro-wires. These protons are confined between MWA units, corresponding to an effective temperature at 813keV. This is beneficial to increase the

nuclear reaction rate R of hydrogen and boron. This work will be beneficial to the research of laser-driven nuclear fusion.

Data availability statement

The original contributions presented in the study are included in the article/supplementary material, further inquiries can be directed to the corresponding authors.

Author contributions

LF wrote the draft of this paper and joined the experiment. TX proposed the idea, took part in the preparation of the draft and led the experiment. QW and JX joined the experiment. GZ provided the MWA target and led the experiment. PW, CF, ZM, and XD joined the experiment. YM discussed the results. SL joined the experiment. XL, JL, RX, and CW operated the laser device. XL and YL provided a professional laser laboratory. BS discussed the results. LJ proposed the idea, took part in the preparation of the draft and is in charge of the project. RL discussed the results. All authors contributed to the article and approved the submitted version.

Funding

This work was supported by the National Natural Science Foundation of China (Grants Nos. 12175299, 11905278, 11975302, 11935008), the CAS Project for Young Scientists in Basic Research (YSBR060) and Youth Innovation Promotion Association of Chinese Academy of Science (No. 2021242).

Conflict of interest

The authors declare that the research was conducted in the absence of any commercial or financial relationships that could be construed as a potential conflict of interest.

Publisher's note

All claims expressed in this article are solely those of the authors and do not necessarily represent those of their affiliated organizations, or those of the publisher, the editors and the reviewers. Any product that may be evaluated in this article, or claim that may be made by its manufacturer, is not guaranteed or endorsed by the publisher.

References

1. Bulanov SV, Khoroshkov VS. Feasibility of using laser ion accelerators in proton therapy. *Plasma Phys Rep* (2002) 28(5):4C53–6. doi:10.1134/1.1478534

2. Roth M, Cowan TE, Key MH, Hatchett SP, Brown C, Fountain W, et al. Fast ignition by intense laser-accelerated proton beams. *Phys Rev Lett* (2001) 86(3):436–9. Epub 2001/02/15. doi:10.1103/PhysRevLett.86.436

3. Remington BA. High energy density laboratory astrophysics. *Plasma Phys Contr F* (2005) 47:A191–A203. doi:10.1088/0741-3335/47/5a/014

4. Snavely RA, Key MH, Hatchett SP, Cowan TE, Roth M, Phillips TW, et al. Intense high-energy proton beams from petawatt-laser irradiation of solids. *Phys Rev Lett* (2000) 85(14):2945–8. Epub 2000/09/27. doi:10.1103/PhysRevLett.85.2945

5. Wilks SC, Langdon AB, Cowan TE, Roth M, Singh M, Hatchett S, et al. Energetic proton generation in ultra-intense laser–solid interactions. *Phys Plasmas* (2001) 8(2): 542–9. doi:10.1063/1.1333697

6. Haberberger D, Tochitsky S, Fiuza F, Gong C, Fonseca RA, Silva LO, et al. Collisionless shocks in laser-produced plasma generate monoenergetic high-energy proton beams. *Nat Phys* (2011) 8(1):95–9. doi:10.1038/nphys2130

7. Shen B, Xu Z. Transparency of an overdense plasma layer. *Phys Rev E Stat Nonlin Soft Matter Phys* (2001) 64(5 Pt 2):056406. Epub 2001/12/12. doi:10.1103/PhysRevE.64.056406

8. Wagner F, Deppert O, Brabetz C, Fiala P, Kleinschmidt A, Poth P, et al. Maximum proton energy above 85 Mev from the relativistic interaction of laser pulses with micrometer thick Ch_{2} targets. *Phys Rev Lett* (2016) 116(20):205002. Epub 2016/06/04. doi:10.1103/PhysRevLett.116.205002

9. Higginson A, Gray RJ, King M, Dance RJ, Williamson SDR, Butler NMH, et al. Near-100 Mev protons via a laser-driven transparency-enhanced hybrid acceleration scheme. *Nat Commun* (2018) 9(1):724. Epub 2018/02/22. doi:10.1038/s41467-018-03063-9

10. Zigler A, Eisenman S, Botton M, Nahum E, Schleifer E, Baspaly A, et al. Enhanced proton acceleration by an ultrashort laser interaction with structured dynamic plasma targets. *Phys Rev Lett* (2013) 110(21):215004. ARTN 215004. doi:10.1103/PhysRevLett.110.215004

11. Ceccotti T, Floquet V, Sgattoni A, Bigongiari A, Klimo O, Raynaud M, et al. Evidence of resonant surface-wave excitation in the relativistic regime through measurements of proton acceleration from grating targets. *Phys Rev Lett* (2013) 111(18):185001. ARTN 185001. doi:10.1103/PhysRevLett.111.185001

12. Ma WJ, Kim IJ, Yu JQ, Choi IW, Singh PK, Lee HW, et al. Laser acceleration of highly energetic carbon ions using a double-layer target composed of slightly underdense plasma and ultrathin foil. *Phys Rev Lett* (2019) 122(1):014803. ARTN 014803. doi:10.1103/PhysRevLett.122.014803

13. Margarone D, Klimo O, Kim IJ, Prokupek J, Limpouch J, Jeong TM, et al. Laser-driven proton acceleration enhancement by nanostructured foils. *Phys Rev Lett* (2012) 109(23):234801. ARTN 234801. doi:10.1103/PhysRevLett.109.234801

14. Qin C, Zhang H, Li S, Wang N, Li A, Fan L, et al. High efficiency laser-driven proton sources using 3d-printed micro-structure. *Commun Phys-uk* (2022) 5(1):124. doi:10.1038/s42005-022-00900-8

15. Gizzi LA, Cristoforetti G, Baffigi F, Brandi F, D'Arrigo G, Fazzi A, et al. Intense proton acceleration in ultrarelativistic interaction with nanochannels. *Phys Rev Res* (2020) 2(3):033451. doi:10.1103/PhysRevResearch.2.033451

16. Dalui M, Kundu M, Trivikram TM, Rajeev R, Ray K, Krishnamurthy M. Bacterial cells enhance laser driven ion acceleration. *Sci Rep-uk* (2014) 4:6002. ARTN 6002. doi:10.1038/srep06002

17. Dozières M, Petrov GM, Forestier-Colleoni P, Campbell P, Krushelnick K, Maksimchuk A, et al. Optimization of laser-nanowire target interaction to increase the proton acceleration efficiency. *Plasma Phys Contr F* (2019) 61(6):065016. doi:10.1088/1361-6587/ab157c

18. Khaghani D, Lobet M, Borm B, Burr L, Gartner F, Gremillet L, et al. Enhancing laser-driven proton acceleration by using micro-pillar arrays at high drive energy. *Sci Rep* (2017) 7(1):11366. Epub 2017/09/14. doi:10.1038/s41598-017-11589-z

19. Vallieres S, Salvadori M, Permogorov A, Cantono G, Svendsen K, Chen Z, et al. Enhanced laser-driven proton acceleration using nanowire targets. *Sci Rep* (2021) 11(1): 2226. Epub 2021/01/28. doi:10.1038/s41598-020-80392-0

20. Feng B, Ji LL, Shen BF, Geng XS, Guo Z, Yu Q, et al. Effects of micro-structures on laser-proton acceleration. *Phys Plasmas* (2018) 25(10):103109. doi:10.1063/1.5037496

21. Curtis A, Hollinger R, Calvi C, Wang S, Huanyu S, Wang Y, et al. Ion acceleration and D-D fusion neutron generation in relativistically transparent deuterated nanowire arrays. *Phys Rev Res* (2021) 3(4):043181. doi:10.1103/PhysRevResearch.3.043181

22. Cristoforetti G, Londrillo P, Singh PK, Baffigi F, D'Arrigo G, Lad AD, et al. Transition from coherent to stochastic electron heating in ultrashort relativistic laser interaction with structured targets. *Sci Rep* (2017) 7(1):1479. Epub 2017/05/05. doi:10.1038/s41598-017-01677-5

23. Jiang S, Ji LL, Audesirk H, George KM, Snyder J, Krygier A, et al. Microengineering laser plasma interactions at relativistic intensities. *Phys Rev Lett* (2016) 116(8):085002. Epub 2016/03/12. doi:10.1103/PhysRevLett.116.085002

24. Moreau A, Hollinger R, Calvi C, Wang S, Wang Y, Capeluto MG, et al. Enhanced electron acceleration in aligned nanowire arrays irradiated at highly relativistic intensities. *Plasma Phys Contr F* (2020) 62(1):014013. doi:10.1088/1361-6587/ab4d0c

25. Shou Y, Kong D, Wang P, Mei Z, Cao Z, Pan Z, et al. High-efficiency water-window X-ray generation from nanowire array targets irradiated with femtosecond laser pulses. *Opt Express* (2021) 29(4):5427–36. Epub 2021/03/18. doi:10.1364/OE.417512

26. Purvis MA, Shlyaptsev VN, Hollinger R, Bargsten C, Pukhov A, Prieto A, et al. Relativistic plasma nanophotonics for ultrahigh energy density physics. *Nat Photon* (2013) 7(10):796–800. doi:10.1038/nphoton.2013.217

27. Jiang S, Link A, Canning D, Fooks JA, Kempler PA, Kerr S, et al. Enhancing positron production using front surface target structures. *Appl Phys Lett* (2021) 118(9):094101. doi:10.1063/5.0038222

28. Pukhov A, Sheng ZM, Meyer-ter-Vehn J. Particle acceleration in relativistic laser channels. *Phys Plasmas* (1999) 6(7):2847–54. doi:10.1063/1.873242

29. Curtis A, Calvi C, Tinsley J, Hollinger R, Kaymak V, Pukhov A, et al. Micro-scale fusion in dense relativistic nanowire array plasmas. *Nat Commun* (2018) 9(1):1077. Epub 2018/03/16. doi:10.1038/s41467-018-03445-z

30. Ceccotti T, Levy A, Popescu H, Reau F, D'Oliveira P, Monot P, et al. Proton acceleration with high-intensity ultrahigh-contrast laser pulses. *Phys Rev Lett* (2007) 99(18):185002. Epub 2007/11/13. doi:10.1103/PhysRevLett.99.185002

31. Fourmaux S, Buffechoux S, Albertazzi B, Capelli D, Lévy A, Gnedyuk S, et al. Investigation of laser-driven proton acceleration using ultra-short, ultra-intense laser pulses. *Phys Plasmas* (2013) 20(1):013110. doi:10.1063/1.4789748

32. Prasad R, Andreev AA, Ter-Avetisyan S, Doria D, Quinn KE, Romagnani L, et al. Fast ion acceleration from thin foils irradiated by ultra-high intensity, ultra-high contrast laser pulses. *Appl Phys Lett* (2011) 99(12):121504. doi:10.1063/1.3643133

33. Bychenkov VY, Singh PK, Ahmed H, Kakolee KF, Scullion C, Jeong TW, et al. Ion acceleration in electrostatic field of charged cavity created by ultra-short laser pulses of 1020–1021 W/Cm2. *Phys Plasmas* (2017) 24(1):010704. doi:10.1063/1.4975082

34. Lu X, Zhang H, Li J, Leng Y. Reducing temporal pedestal in a Ti:sapphire chirped-pulse amplification system by using a stretcher based on two concave mirrors. *Opt Lett* (2021) 46(21):5320–3. Epub 2021/11/02. doi:10.1364/OL.435145

35. Wang X, Han G-R. Fabrication and characterization of anodic Aluminum Oxide template. *Microelectronic Eng* (2003) 66(1-4):166–70. doi:10.1016/s0167-9317(03)00042-x

36. Mancic A, Fuchs J, Antici P, Gaillard SA, Audebert P. Absolute calibration of photostimulable image plate detectors used as (0.5-20 Mev) high-energy proton detectors. *Rev Sci Instrum* (2008) 79(7):073301. Epub 2008/08/07. doi:10.1063/1.2949388

37. Kemp AJ, Wilks SC, Hartouni EP, Grim G. Generating kev ion distributions for nuclear reactions at near solid-density using intense short-pulse lasers. *Nat Commun* (2019) 10(1):4156. Epub 2019/09/15. doi:10.1038/s41467-019-12076-x

38. Schnürer M, Andreev AA, Steinke S, Sokollik T, Paasch-Colberg T, Nickles PV, et al. Comparison of femtosecond laser-driven proton acceleration using nanometer and micrometer thick target foils. *Laser Part Beams* (2011) 29(4):437–46. doi:10.1017/s0263034611000553

39. Derouillat J, Beck A, Pérez F, Vinci T, Chiaramello M, Grassi A, et al. Smilei: A collaborative, open-source, multi-purpose particle-in-cell code for plasma simulation. *Comput Phys Commun* (2018) 222:351–73. doi:10.1016/j.cpc.2017.09.024

40. Andreev AA, Steinke S, Sokollik T, Schnürer M, Avetsiyan ST, Platonov KY, et al. Optimal ion acceleration from ultrathin foils irradiated by a profiled laser pulse of relativistic intensity. *Phys Plasmas* (2009) 16(1):013103. doi:10.1063/1.3054528

41. Gitomer SJ, Jones RD, Begay F, Ehler AW, Kephart JF, Kristal R. Fast ions and hot electrons in the laser–plasma interaction. *Phys Fluids* (1986) 29(8):2679. doi:10.1063/1.865510

42. Zou DB, Pukhov A, Yi LQ, Zhuo HB, Yu TP, Yin Y, et al. Laser-driven ion acceleration from plasma micro-channel targets. *Sci Rep* (2017) 7:42666. Epub 2017/02/22. doi:10.1038/srep42666